Tony Shi[1]
Systems and Artificial Intelligence Laboratory,
Machine Tool Research Center,
University of Tennessee, Knoxville,
Knoxville, TN 37996
e-mail: tony.shi@utk.edu

Jiajie Wu
Systems and Artificial Intelligence Laboratory,
Machine Tool Research Center,
University of Tennessee, Knoxville,
Knoxville, TN 37996
e-mail: jwu71@vols.utk.edu

Mason Ma
Systems and Artificial Intelligence Laboratory,
Machine Tool Research Center,
University of Tennessee, Knoxville,
Knoxville, TN 37996
e-mail: hma19@vols.utk.edu

Elijah Charles
Machine Tool Research Center,
University of Tennessee, Knoxville,
Knoxville, TN 37996
e-mail: echarle4@vols.utk.edu

Tony Schmitz
Fellow ASME
Machine Tool Research Center,
University of Tennessee, Knoxville,
Knoxville, TN 37996;
Manufacturing Science Division,
Oak Ridge National Laboratory,
Oak Ridge, TN 37830
e-mail: tony.schmitz@utk.edu

AFSD-Nets: A Physics-Informed Machine Learning Model for Predicting the Temperature Evolution During Additive Friction Stir Deposition

This study models the temperature evolution during additive friction stir deposition (AFSD) using machine learning. AFSD is a solid-state additive manufacturing technology that deposits metal using plastic flow without melting. However, the ability to predict its performance using the underlying physics is in the early stage. A physics-informed machine learning approach, AFSD-Nets, is presented here to predict temperature profiles based on the combined effects of heat generation and heat transfer. The proposed AFSD-Nets includes a set of customized neural network approximators, which are used to model the coupled temperature evolution for the tool and build during multi-layer material deposition. Experiments are designed and performed using 7075 aluminum feedstock deposited on a substrate of the same material for 30 layers. A comparison of predictions and measurements shows that the proposed AFSD-Nets approach can accurately describe and predict the temperature evolution during the AFSD process. [DOI: 10.1115/1.4065178]

1 Introduction

Additive friction stir deposition (AFSD) has emerged as a novel, solid-state metal additive manufacturing (AM) technology with the potential for broad application. AFSD is a plasticity-based, solid-state AM process where no melting occurs, and the geometry and microstructure are produced during layer-by-layer severe plastic deformation. This is fundamentally different from the solidification mechanism observed during fusion-based AM technologies in which the materials are melted using a high-intensity heat source [1,2]. AFSD can, therefore, provide superior mechanical and material properties, including lower porosity, reduced thermal gradients, lower residual stress, and uniform and homogeneous microstructure

[3]. These advantages make AFSD an attractive choice for the defense and aerospace industries, for example.

Prior AFSD studies have considered both the process and build material characteristics. For process efforts, AFSD has been combined with machining and metrology while considering the hybrid manufacturing processes holistically to arrive at a comprehensive approach to process planning [4–6]. It provides a new option for the emerging hybrid manufacturing approach to reduce material use and removal [7,8]. For materials, researchers have deposited multiple materials, including aluminum alloys [9–12], pure copper [13], magnesium alloys [14,15], stainless steel [16], and titanium alloys [17]. Various process control parameters, including spindle speed, material feed rate, and traverse speed, have been investigated to understand their impact on deposition [4,18]. Process topics include temperature [15], plastic strain [10], residual stress [11,19], morphology and microstructure [10,12–14,16,17,20,21], and material flow [22].

---

[1]Corresponding author.

It is understood that the complex coupled thermomechanical behaviors, severe plastic deformation, and multiple process control parameters present a significant challenge for AFSD modeling research [9,18,23–28]. The peak temperatures of Cu and Al-Mg-Si during AFSD were empirically modeled as power law relationships with respect to spindle speed and traverse speed [18]. Multi-physics-coupled thermomechanical process models have also been presented. For example, coupled thermomechanical mesh-free models based on smoothed particle hydrodynamics (SPH) have been applied to simulate the temperature, build profile, and plastic strain for AFSD [23]. Researchers have compared material constitutive models [24] and combined computational and experimental approaches to explore particle tracking [25]. Mesh-based modeling efforts include the finite volume method (FVM) for heat influx and outflux analysis [26], computational fluid dynamics (CFD) for material flow and thermomechanical processing history [27], the finite element method (FEM) for the stress induced by spatial nonuniformity of dynamic bulk modulus [9], a multi-layer FEM for explaining the microstructure using spatial and temporal prediction of temperature [28], and a multi-layer FEM in Ref. [29] for linking process parameters to microstructure. A comprehensive review of AFSD research from the perspective of process-structure-property-performance convergence is presented in Ref. [30].

However, these high-fidelity process models are still in their early stages of development. Current limitations include instability with boundary conditions (such as significant viscosity differences between the build material and atmosphere), high computational cost (36 h of computation for a single-layer deposition simulation has been reported [23]), and poor scalability for multi-layer depositions (most studies focus on a single layer with a few exceptions). This poses challenges for real-time prediction, control, and optimization, as well as scalability to production-level part manufacturing using multi-layer depositions and complicated tool paths.

In terms of machine learning (ML) modeling efforts, only a few recent studies have investigated tool temperature modeling using neural networks [31]. Besides, a growing research focus is on physics-informed machine learning (PIML) that combines existing physical knowledge with data such that the acquired ML models can better respect physical laws [32]. Prior PIML approaches can be classified into the following categories: (1) physics-informed neural networks (PINN) that integrate the governing equations into the neural network (NN) loss function as soft constraints [33] or hard constraints [34]; (2) physics-informed features construction for ML model input [35,36]; and (3) physics information incorporated into the ML model structure design [37]. However, these PIML approaches are generally designed for a single physical process, which is described by a specific set of governing equations. While the AFSD process is a multi-stage and multi-physics additive manufacturing process that involves mechanical inputs, multiple thermal cycles, heat generation, cooling, and heat transfer, the above PIML approaches cannot be directly applied to the studied AFSD modeling.

This study focuses on two physical phenomena determining temperature evolution during AFSD: *heat generation* (at the tool deposition surface) and *heat transfer* (between the tool, build, and substrate). Currently, the underlying physics of heat generation and heat transfer processes with respect to process parameters are not well understood. This study investigates the fundamental functional relationships between heat generation and heat transfer to accurately describe temperature evolution during AFSD. This represents the first attempt at modeling AFSD temperature evolution using ML and in-process data signals. The primary contributions are the following:

(1) A physics-informed machine learning approach, AFSD-Nets, is developed to model the heat generation and heat transfer during AFSD. Process decomposition based on the process parameters and physical variables is used to describe heat generation and heat transfer during a thermal cycle.

These thermal stages and the location-based, time-delay phenomenon for heat transfer are incorporated into AFSD-Nets as underlying physics embedded in the in-process data to improve the model accuracy.

(2) The proposed AFSD-Nets accurately predicts the temperature evolution due to heat generation and heat transfer using in-process data from a 30-layer deposition. The computation time is 5 min. This shows the accuracy and efficiency of the proposed AFSD-Nets approach in comparison to existing multi-physics process models. Additionally, the ML models can be integrated into the current multi-physics process modeling framework as thermal model surrogates.

(3) It is demonstrated that the AFSD-Nets models are generalizable using coupled time domain simulation. Given process parameters and initial temperatures, the simulation can predict the tool and the build temperature evolution during AFSD. This shows the effectiveness of the models in capturing the underlying physics and their potential use for AFSD control and optimization.

The paper is organized as follows: In Sec. 2, AFSD is described, and the temperature evolution due to heat generation and heat transfer is introduced. Section 3 presents the AFSD-Nets design using distinct stages of heat generation and heat transfer for both the tool and the build. The experimental setup for depositing an aluminum alloy on an aluminum substrate and collecting data is described in Sec. 4. The numerical results of the proposed AFSD-Nets are presented in Sec. 5. For experimental validation, additional physical and numerical experiments for the proposed AFSD-Nets and its acquired models are presented in Sec. 6. Section 7 provides conclusions and the research outlook.

2 AFSD Temperature Evolution

This section describes the heat generation and heat transfer, which determine the temperature evolution in AFSD. Based on this, the strategy for modeling the underlying heat generation and heat transfer physics as functions of the process parameters is presented.

The AFSD temperature evolution is described in Fig. 1. At the beginning of each layer's deposition, the tool is moved downward toward the substrate, leaving a small gap between the tool and the substrate. The square feed rod (9.53 mm side length by 508 mm axial length) is forced downward by a ball screw actuator at the selected material feed rate through the hollow, rotating tool. This generates frictional heating at the substrate interface, which increases the local temperature and reduces the feed rod strength sufficiently to cause plastic flow and a metallurgical bond with the substrate or previous layer. The tool is subsequently traversed along the programmed path using the selected traverse speed to deposit material in a layer-by-layer fashion.

Heat generation can be divided into two general stages: heating and deposition. In the heating stage, the heat is generated mainly by the contact friction between the extruded material and the tool bottom and substrate top surfaces. The temperature increases with spindle speed due to increased power input. Once the temperature reaches the desired level (based on the temperature-dependent material strength), the spindle speed is reduced, and the deposition stage begins. The heat is then generated at a relatively slower rate due to the (typically) lower spindle speed during deposition.

The time-dependent heat transfer is the result of heat generation at the moving heat source from one layer to the next. The heat is conducted away from both the tool and the build during the entire AFSD process. This conduction includes two stages: layer deposition and after layer deposition. The former stage corresponds to a moving heat source, while the latter relates to the initial conditions and specific locations on the build.

Figure 2 displays the temperature evolution induced by heat generation and heat transfer. The data represent two layers of a 30-layer
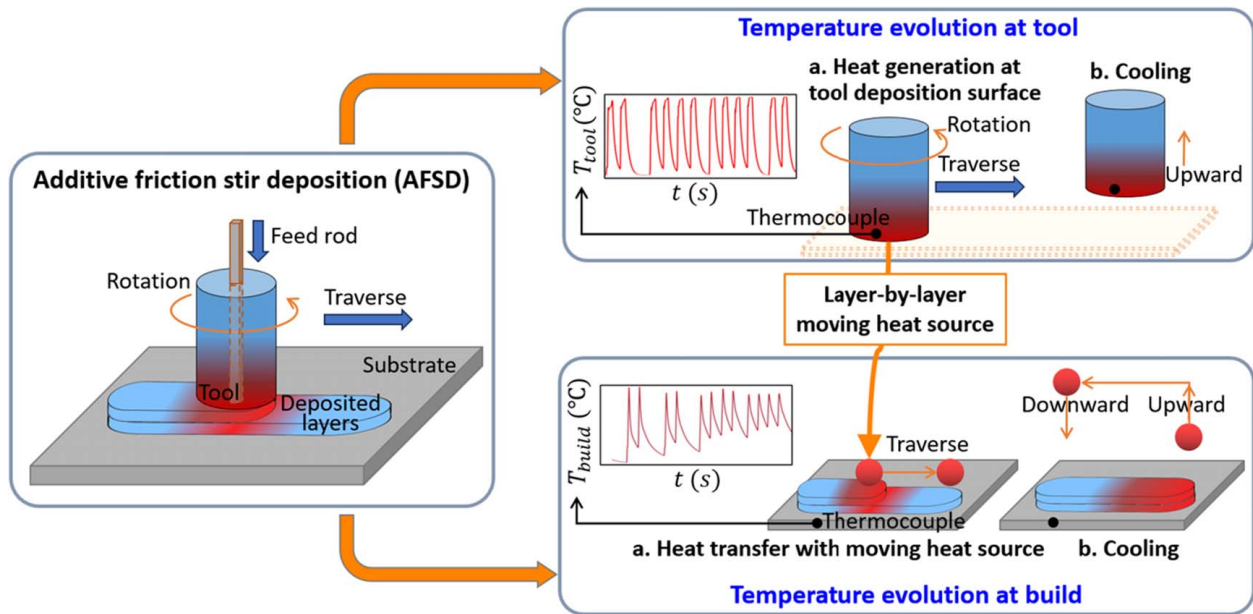
Fig. 1 AFSD temperature evolution consists of heat generation and heat transfer. Heat is generated by friction at the tool deposition surface and plastic deformation within the material (adiabatic heating). During layer-by-layer deposition, heat conducts away from this moving heat source to the build and substrate. Thermal cycling is observed in the tool deposition temperature profiles due to discrete deposition intervals.

deposition obtained using the experimental setup described in Sec. 4. The temperatures from the thermocouples embedded in the tool and substrate are shown as a function of deposition time. The heat generation and transfer stages are identified. The time-delay heat transfer from the moving heat source to the four K-type thermocouples in the substrate is also observed.

In this study, a process decomposition is performed to isolate the data due to heat generation and heat transfer by separating the time series into segments. Figures 2(b) and 2(c) show the process decomposition using spindle torque and the tool's axial location. Heat generation at the tool deposition surface begins when the rotating tool moves downward to provide contact between the feedstock and the build (i.e., the tool's axial location is the current build thickness), and the spindle torque increases. On the contrary, tool cooling begins when the tool leaves the build, and the spindle torque decreases.

In this context, the fundamental research question for this study is: What are the functional relations of heat generation and heat transfer that can accurately describe the temperature evolution during AFSD? The approach is to design a physics-informed machine learning model for AFSD to identify these relations using in-process data. Technical solutions, the experimental setup, and the research findings are presented in the following sections.

3 Proposed AFSD-Nets

This section presents the proposed physics-informed ML approach, AFSD-Nets, for modeling the temperature evolution during AFSD. An overview of AFSD-Nets is first presented. This is followed by its component design for temperature evolution at tool and build. The models identified by AFSD-Nets are then applied in coupled time domain simulation.

3.1 Overview of AFSD-Nets. The main idea of AFSD-Nets is to model each of the heat generation, cooling, and heat transfer stages with a distinct neural network and then couple them to model temperature evolution during the entire AFSD process. AFSD-Nets is a PIML approach because it is established based on the physical process decomposition and coupling of AFSD.

Because the AFSD process is a multi-stage and multi-physics additive manufacturing process, a single PIML model cannot capture all the underlying temperature evolution patterns for the heat generation, cooling, and heat transfer stages. AFSD-Nets incorporates the physical knowledge of multi-stage and multi-physics processes into the design of multiple networks that have causal relationships with each other. Within each network, physical knowledge is also incorporated as the input features like, for example, the Euclidean distance between the tool and the build, which is calculated as an input feature for modeling heat transfer from the tool to the build.

Figure 3 displays an overview of the proposed AFSD-Nets approach. Underlying physics during AFSD, including the thermal cycle, process decomposition of heat generation and heat transfer, and location-based time-delay phenomenon for heat transfer at the build are incorporated into the design of the ML models. Customized neural networks can, therefore, be built for each stage of heat generation and heat transfer as follows. For temperature evolution at the tooltip, networks for heat generation at the tool deposition surface and tool cooling are developed. For deposition temperature evolution, a mask mechanism on the features is applied for the build heat transfer network to indicate the existence of the moving heat source or not. These neural networks are trained and optimized individually using the in-process data based on the time segment where the specific thermal process occurs. The set of learned networks by AFSD-Nets are coupled to perform the time domain simulation of temperature evolution during AFSD. The simulation output of the tool heat generation network is used to set initial conditions of the tool cooling network simulation, and vice versa, to fully describe the temperature evolution at the tooltip. The tooltip temperature prediction is then used as input to the heat transfer network. Due to the mask mechanism, a unified network model is learned and used for simulating the heat transfer at the build. The combined outcomes propagate to describe and predict the temperature evolution during multi-layer material deposition.

3.2 Heat Generation and Tool Cooling Networks for Modeling Tool Temperature Evolution. The heat generation stage begins at the tool surface during deposition, and then tool cooling begins when the tool leaves the build, and the spindle
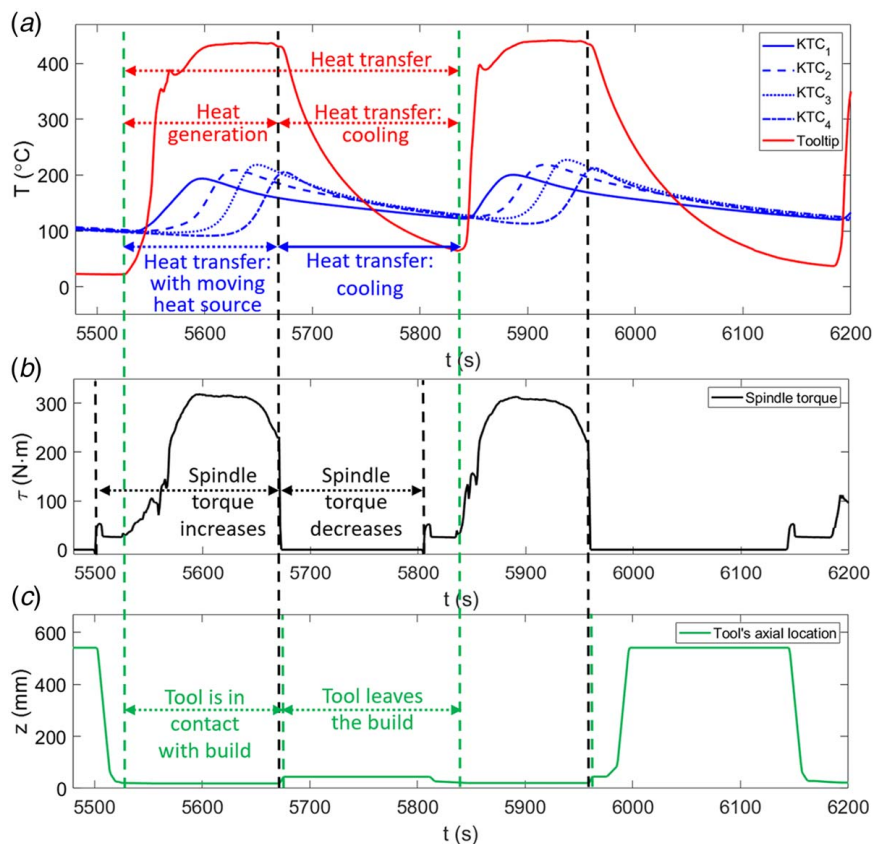
Fig. 2 Temperature evolution induced by heat generation and heat transfer. Data are from two layers of a 30-layer deposition using the experiment setup in Sec. 4. (*a*) Process decomposition of temperature evolution at the tooltip and the build using spindle torque in (*b*) and the tool's axial location in (*c*). Tooltip temperature was measured by a thermocouple embedded in the rotating tool, and the build temperatures were measured using four K-type thermocouples (KTC) in the substrate. (*b*) Data are separated by whether the spindle torque is applied or removed. (*c*) Data are separated by the tool's axial location. Heat generation begins when the rotating tool is in contact with the build, and the spindle torque increases. Cooling begins when tool leaves the build, and the spindle torque decreases.
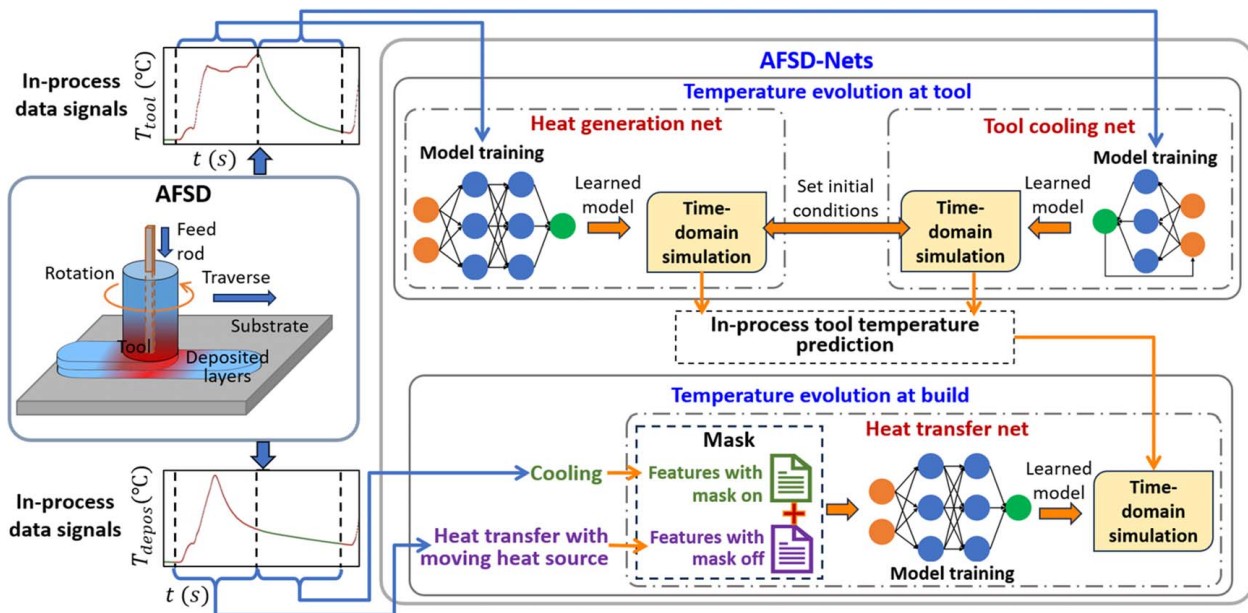

Fig. 3 Overview of the proposed AFSD-Nets as a set of customized neural networks informed by the underlying physics during AFSD. Each network models a specific thermal stage of heat generation and heat transfer. The coupled time domain simulation describes and predicts the temperature evolution during AFSD.

torque subsequently decreases. The heat generation network and tool cooling network are developed to model the time-dependent tool temperature. The coupled heat generation and tool cooling determine the tool temperature evolution during AFSD.

One thermal cycle of the tool during AFSD consists of the heat generation and tool cooling stages. For any thermal cycle, let P_{heat} and P_{cool} denote the process windows for heat generation and tool cooling throughout. It is assumed that the tooltip and deposition surface temperatures are equal during the heat generation stage. Let $T(t)$ denote the temperature at time t and $T(t - \Delta t)$ denote the temperature at time $t - \Delta t$ throughout this paper.

3.2.1 Heat Generation Network.

The heat generation stage in any thermal cycle can be described as an unknown dynamical system with control, where $t \in P_{\text{heat}}$. Let $\boldsymbol{u}(t) = [\boldsymbol{u}_1(t), \boldsymbol{u}_2(t)]$ denote the vector of in-process control variables, where $\boldsymbol{u}_1(t)$ is the vector of process parameters that can be explicitly selected and controlled, such as tool spindle speed, feedstock and tool feed velocities. $\boldsymbol{u}_2(t)$ includes process physical variables that cannot be explicitly selected but can be measured, such as spindle torque and actuator force to push the feedstock through the rotating spindle. The following heat generation network is proposed

$$T_{\text{tool}}(t) = \mathcal{N}_{\text{heat\_gen}}(\boldsymbol{u}(t - \Delta t), T_{\text{tool}}(t - \Delta t)), \ t \in P_{\text{heat}}$$

where $\mathcal{N}_{\text{heat\_gen}}(\cdot)$ is the standard fully connected neural network with several hidden layers, each defined in the form $h = \sigma(wh + b)$. Here, w represents the weights from the preceding hidden layer to the current one, and b represents the bias. The activation function $\tanh(\cdot)$ is used to account for non-linearity

$$\sigma(x) = \tanh(x) = \frac{e^x - e^{-x}}{e^x + e^{-x}}$$

For the output layer, only the linear combination of the last hidden layer is applied as $T_{\text{tool}}(t)$. The determination of the input for the mapping, the network structure, and the weights within the model should be established based on the physical knowledge and available data. A grid search, combined with validation techniques, is employed for this purpose. The required temperature data is obtained using a thermocouple embedded in close proximity to the tooltip. The heat generation network is used to identify a direct relationship between the temperature and other in-process data during the heat generation stage.

3.2.2 Tool Cooling Network.

The tool cooling network is developed to model the tool cooling stage, where $t \in P_{\text{cooling}}$ for any thermal cycle. The initial state of heat generation plays a crucial role in multi-layer deposition during AFSD. In conjunction with the heat generation network, the tool cooling network aids in determining the initial condition for the heat generation stage of the next thermal cycle. The proposed tool cooling network is

$$T_{\text{tool}}(t) = \mathcal{N}_{\text{tool\_cool}}(T_{\text{tool}}(t - \Delta t), T_{\text{room}}), \ t \in P_{\text{cool}}$$

where T_{room} denotes the room temperature. The tool cooling network $\mathcal{N}_{\text{tool\_cool}}(\cdot)$ is the classical Nonlinear Autoregressive with Exogenous Inputs (NARX) network that aligns with commonly used neural network structures in heat transfer.

Coupling the heat generation network and tool cooling network, we have

$$T_{\text{tool}}(t) = \begin{cases} \mathcal{N}_{\text{heat\_gen}}(\boldsymbol{u}(t - \Delta t), T_{\text{tool}}(t - \Delta t)), & t \in P_{\text{heat}} \\ \mathcal{N}_{\text{tool\_cool}}(T_{\text{tool}}(t - \Delta t), T_{\text{room}}), & t \in P_{\text{cool}} \end{cases}$$

This equation can be used to model the tool temperature evolution for all thermal cycles during AFSD.

3.3 Heat Transfer Network for Modeling Build Temperature Evolution.

The build temperature evolution is caused by heat transfer during the layer-by-layer deposition and subsequent thermal cycling. To accurately model the build temperature evolution, three important factors should inform the ML method: (1) the build geometry changes layer by layer; (2) the presence or absence of the moving heat source results in two distinct heat transfer mechanisms; and (3) there is a time delay between deposition events. In particular, the process decomposition within a single thermal cycle is insufficient to describe the time-delay phenomenon. This motivates the design of a unified neural network, the heat transfer network, for modeling build temperature evolution during AFSD.

3.3.1 Heat Transfer Network.

The heat transfer network establishes a mapping between the moving heat source and the build temperature at a specific location.

Three input features are selected to develop the heat transfer network. They are the Euclidean distance d between the tool and target location on the build, the tool temperature $T_{\text{tool}}(t - \Delta t)$ at time $t - \Delta t$, and the build temperature $T_{\text{build}}^{\boldsymbol{c}_b}(t - \Delta t)$ at location $\boldsymbol{c}_b$ and time $t - \Delta t$. The distance d is given by

$$d(\boldsymbol{c}_t, \ \boldsymbol{c}_b) = \sqrt{(x_{\text{tool}} - x_{\text{build}})^2 + (y_{\text{tool}} - y_{\text{build}})^2 + (z_{\text{tool}} - z_{\text{build}})^2}$$

where $\boldsymbol{c}_t = [x_{\text{tool}}, y_{\text{tool}}, z_{\text{tool}}]$ and $\boldsymbol{c}_b = [x_{\text{build}}, y_{\text{build}}, z_{\text{build}}]$ refer to the coordinates of the tool and any target build location, respectively. The build geometry information is contained in this feature. To accommodate the two distinct heat transfer mechanisms caused by the presence or absence of the moving heat source, a mask function is introduced

$$\text{Mask}(d, T_{\text{tool}}(t - \Delta t)) = \begin{cases} (d, T_{\text{tool}}(t - \Delta t)), & t \in P_{\text{heat}} \\ (d_{\text{mask}}, T_{\text{mask}}), & t \in P_{\text{cool}} \end{cases}$$

When the moving heat source is present ($t \in P_{\text{heat}}$), the features d and $T_{\text{tool}}(t - \Delta t)$ are active. However, when the moving heat source is not present ($t \in P_{\text{cool}}$), these two features are irrelevant. For any $t \in P_{\text{cool}}$, d_{mask} and T_{mask} are set as the predefined constants to eliminate their influence. With this mask function, the heat transfer network is given by

$$T_{\text{build}}^{\boldsymbol{c}_b}(t) = \mathcal{N}_{\text{heat\_trans}}(\text{Mask}(d, T_{\text{tool}}(t - \Delta t)), T_{\text{build}}^{\boldsymbol{c}_b}(t - \Delta t)),$$
$$t \in P_{\text{heat}} \cup P_{\text{cool}}$$

where $\mathcal{N}_{\text{heat\_trans}}(\cdot)$ is a standard fully connected neural network. This unified equation can be used to model the build temperature evolution for all thermal cycles during AFSD.

The mask function establishes the heat transfer network as a unified neural network approximator for build temperature evolution, with the ability to capture the time-delay phenomenon across multiple thermal cycles. After training, the heat transfer network can predict the temperature evolution of a given location $\boldsymbol{c}_b$ on the build.

It is noted that the basic components and operators used for the neural network models are by default. Each neural network is trained by minimizing the mean squared error (MSE) using the backpropagation algorithm

$$\text{MSE} = \frac{1}{n} \|\mathcal{N}(\cdot) - T(\cdot)\|_2^2$$

where n is the number of samples used for updating the weights of the corresponding network.

3.4 Coupled Time Domain Simulations for Tool and Build.

Let $T_{\text{tool}}^*(t)$ and $T_{\text{build}}^{*\boldsymbol{c}_b}(t)$ denote the learned models for the tool and build by AFSD-Nets. After all neural networks in AFSD-Nets are trained, they are coupled to execute a time domain simulation for predicting the time-dependent AFSD temperature, as described by Algorithm 1 in Table 1. The coupled thermal behaviors of heat generation and heat transfer between the tool, build, and substrate determine the interconnectivity between these three networks. The final value from the heat generation simulation is used as the

Table 1   Algorithm procedure of time domain simulation using AFSD-Nets models

Algorithm 1. Time domain simulation using AFSD-Nets models	
Input:	Learned models: $T^*_{\text{tool}}(t)$, and $T^{*c_b}_{\text{build}}(t)$.
	Process control parameters: $\boldsymbol{u}(t)$ in the form of in-process data.
	Number of deposition layers: L. Let l be the index of the current deposition layer.
	Initial conditions: Given $T^{*1}_{\text{tool}}(0)$ when deposition begins at the first layer, $T^{*c_b}_{\text{build}}(0)$, is the initial temperature of location $\boldsymbol{c}_b$ at build.
Step 1.	Execute time domain simulation for tool temperature. Set $l=1$.
	while($l \le L$):
1.1	Execute simulation for heat generation at lth layer by $T^{*l}_{\text{tool}}(t)$ with initial value $T^{*l}_{\text{tool}}(0)$, when $t \in P_{\text{heat\_gen}}$;
1.2	Use final value of $T^{*l}_{\text{tool}}(t)$ as initial value to execute simulation for tool cooling at lth layer by $T^{*l}_{\text{tool}}(t)$, when $t \in P_{\text{cooling}}$;
1.3	Update $T^{*(l+1)}_{\text{tool}}(0)$ by the final value of $T^{*l}_{\text{tool}}(t)$; $l=l+1$.
Step 2.	$T^{*l}_{\text{tool}}(t) \leftarrow$ Prediction of in-process tool temperature for all layers.
Step 3.	Execute time domain simulation for build temperature.
	For a given location $\boldsymbol{c}_b$ at build:
	Execute simulation for heat transfer at build by $T^{*c_b}_{\text{build}}(t)$ using the initial condition $T^{*c_b}_{\text{build}}(0)$ and tool temperature prediction $T^{*l}_{\text{tool}}(t)$;
Output:	Prediction of tool temperature evolution $T^*_{\text{tool}}(t)$, and prediction of build temperature evolution $T^{*c_b}_{\text{build}}(t)$ at location $\boldsymbol{c}_b$.

initial value for the following tool cooling simulation and vice versa (Step 1). After the tool temperature simulation is completed, the in-process tool temperature prediction for all layers is stored (Step 2). For each build location, the build temperature is predicted by the heat transfer network using the initial condition and tool temperature prediction (Step 3). In this sense, the coupled interconnectivity makes AFSD-Nets the state-space representation of the thermal dynamical system during AFSD, which can simulate the entire temperature evolution. This is important for the practical use of the learned models to perform offline simulations that predict the temperature evolution due to different process parameters. This information can be used to define operating parameters in a pre-process sense. Further control and optimization of AFSD can also be potentially developed based on this accurate and computationally efficient coupled time domain simulation.

4   Experimental Setup

A commercially available MELD Manufacturing L3 machine was used to deposit solid wrought aluminum 7075 feedstock rod with $9.53\,\text{mm} \times 9.53\,\text{mm} \times 508\,\text{mm}$ dimensions on the aluminum 7075 substrate. Deposition was performed to build a wall with a length of 216 mm and height of 45 mm (30 layers with each layer 1.5 mm thickness). Deposition was performed in a single direction, and the tool was returned to the same starting position for each layer. Given the wall length, a single rod of wrought stock was able to deposit two layers before the next rod was inserted into the spindle (i.e., the L3 is a discrete deposition machine where each rod must be manually loaded). The time required to insert the next rod was 2–3 min. To maintain consistent starting conditions for each layer, an artificial interval of 2 min was inserted after the first deposition layer for each rod to mimic the time interval for refilling. The result was 30 individual deposition layers that each had a similar initial temperature for the tool, substrate, and build.

The operating parameters were 135 rpm spindle speed during deposition, 115.6 mm/min material feed rate, and 127 mm/min tool feed rate (traverse speed). To begin each layer, the spindle speed was set at 350 rpm to heat the material and was reduced to 135 rpm as the deposition began. A cooling jacket located around the tool was run at a constant flowrate during deposition to cool the tool and avoid excessive heating of the rod within the tool, which can cause the deposition to fail due to adhesion between the rod and the tool's internal passage. After the numerical results in Sec. 5 were obtained, additional experiments using a different spindle speed of 115 rpm were performed for further experimental validation. See details in Sec. 6.

Time series data (spindle speed, torque, and power; material feed rate and actuator force and torque; and position, velocity, and torque for the X, Y, and Z axes) were recorded by the L3 controller using a 1 Hz sampling rate. The IR camera temperature data were sampled

separately, as shown in Fig. 4(a). The tool thermocouple embedded in the rotating tool (a MELD Manufacturing product) was located within 0.25–0.38 mm of the tool surface and was used to measure the tool–deposit interface temperature. A FLIR 70 infrared camera was attached to the moving spindle carriage. The peak temperature within the field of view was sampled at 30 Hz. Black tape was wrapped around the tool head to approximate black body emissivity. The IR camera and the tool-embedded thermocouple temperatures were compared to confirm the performance of the two sensors.

For the substrate temperature, two baseplates were used. The upper baseplate was the one where the deposit was made, and four equally spaced K-type thermocouples were embedded 2.54 mm below the build surface and along the track direction from the underside of this plate. Figure 4(b) shows the locations of the four thermocouples. The end of the plate nearest the deposit start is marked with an "S," the end closest to the deposit end is marked with an "E," and the intermediate distance between two adjacent thermocouples was 58.5 mm. The underside in Fig. 4(b) was covered by the lower baseplate to protect the thermocouples.

The experiments resulted in 11,358 in-process data points. The number of data points from each layer is different. For each layer, the number of data points collected at the heat generation stages varies from 136 to 178, and the number of data points collected at the cooling stage varies from 149 to 634. This can be caused by variations in the time for manually loading feedstock and in the waiting time between the deposition of each layer to satisfy the work condition before it starts to traverse. The features include the L3 controller-captured data (spindle speed, torque, and power; material feed rate and actuator force and torque; and position, velocity, and torque for the X, Y, and Z axes), the tooltip temperature from the embedded thermocouple, and the temperatures from the four substrate thermocouples. Additionally, the 341,606 data points obtained by the IR camera were used to validate the embedded thermocouple temperature, demonstrating good agreement between the two. For the subsequent analysis, the temperature data from the embedded thermocouple was used to represent the tooltip temperature.

5   Computational Experiments

In this section, the numerical results and analysis of the proposed AFSD-Nets are presented. The in-process data obtained using the experimental setup shown in Sec. 4 were used to train and test the model. The AFSD-Nets models are first validated to confirm good accuracy. Then time domain simulations are performed to show the effectiveness of the learned models in predicting the entire temperature evolution at the tool and build during AFSD. All computations are completed using PYTHON and executed using
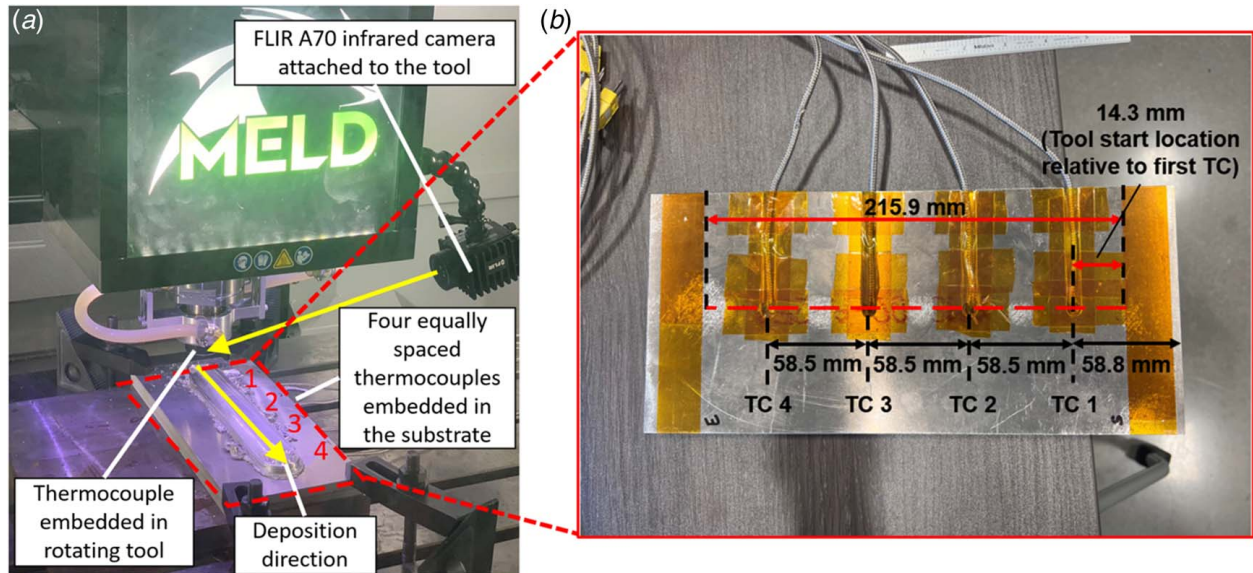
Fig. 4 Experimental setup for depositing 7075 aluminum feed rod on a 7075 aluminum substrate for 30 layers using the MELD Manufacturing L3 machine. (*a*) A thermocouple embedded in the tool was used to measure the tool temperature near the deposition interface. A FLIR A70 infrared camera was attached to the spindle carriage to measure the external temperature at the tooltip. Four equally spaced thermocouples were embedded in the substrate for measuring temperature evolution beneath the deposition track. (*b*) Substrate with locations of the four thermocouples. The location nearest the deposit start is marked with an "S," and the location nearest the deposit end is marked with an "E."

an AMD Ryzen 7 5800X @3.80 GHz, 32 GB Memory, 64-bit Windows operating system, and eight cores with 16 logical processors. Note the CPU computation is reported as there was no significant difference between the computational times when selecting GPU or CPU implementations for the simple neural network structures applied in AFSD-Nets.

5.1 Parameter Settings of AFSD-Nets. The model structures and training for AFSD-Nets are as follows. The dataset is split into training, validation, and test sets, with a split ratio of 20:5:5 layers, respectively. Process decomposition based on spindle torque and the tool's axial position, as described in Sec. 2, is performed to separate each layer into heat generation and cooling stages. For the heat generation stage of each layer, the first 20 measurements are truncated. The input data are normalized using min-max normalization to mitigate the impact of varying magnitudes, while the output data undergo a logarithmic transformation to reduce parameter sensitivity. For the tool heat generation network, a grid search for the nine model structures consisting of the number of hidden layers selected from the set [1, 2, 3] and the number of nodes in each hidden layer chosen from the set [8, 10, 16] is performed. For the tool cooling network, a fixed NARX network structure is employed after a preliminary grid search, which is not presented for brevity. The model structure is set as [2, 4, 1], which consists of two input nodes, one hidden layer with four nodes, and one output node. Other parameters use default settings in the adopted NARX network operated by the MATLAB engine on the PYTHON platform.

For build temperature evolution, the entire dataset is first processed by the Mask($\cdot$) function for setting the distance and tool temperature values. The values for (d_{mask}, T_{mask}) must be less than the smallest values of distance and tool temperature within the entire dataset. This is to ensure these two features do not affect the network training when the tool leaves the build ($t \in P_{cool}$) while maintaining the underlying physics defined by the data scale when the tool is on the build ($t \in P_{heat}$). After this, the min-max normalization is used as $x' = (x - x_{min})/(x_{max} - x_{min})$, where x and x' are the original and scaled values of distance or tool temperature, and x_{min} and x_{max} are the minimum and maximum values within the dataset, respectively. In this paper, (d_{mask}, T_{mask}) = (-2, -100) is set, considering the

ranges of distance $d \in [0.16,\ 8.13]$ mm and the tool temperature $T_{tool} \in [20.3,\ 447.8]°$C in the dataset. In addition, only training data from the first three thermocouples (KTC1, KTC2, and KTC3) are stacked as a single dataset for training, while the last thermocouple near the end of the build (KTC4) is used for validation of the extrapolation capability of the learned model. The model structure is set as [3, 10, 10, 10, 1] (three input nodes, three hidden layers each with ten nodes, and one output node) after a preliminary grid search, which is not presented for brevity.
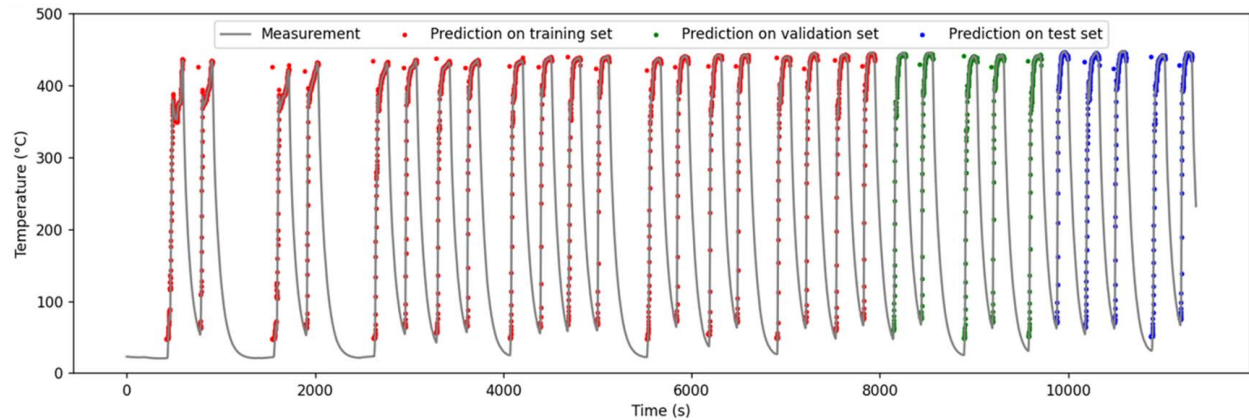
5.2 Validation of Learned Models. Each network of AFSD-Nets is trained using the settings stated in Sec. 5.1. The training time for AFSD-Nets (single execution without grid search) is less than 5 min, with about 1 min, 30 s, and 3 min for the tool heat generation network, tool cooling network, and heat transfer network at build, respectively. The learned models are validated in this section before the time domain simulation is completed.

5.2.1 Model Validation for Tool Temperature Evolution. For the heat generation network at the tool deposition surface, two sets of input features are employed depending on which process control parameters are used. The first learned model $\mathcal{N}_{heat\_gen}(3)$ considers three features, including the time-delay tool temperature, spindle speed, and material feed rate. This makes the learned $\mathcal{N}_{heat\_gen}(3)$ independent of other in-process signals and available for offline time domain simulation of heat generation, given the process parameter values along the path. The second learned model $\mathcal{N}_{heat\_gen}(6)$ considers six features, including the time-delay tool temperature, the in-process signals spindle torque, feed actuator torque, and feed actuator force, as well as spindle speed and material feed rate. The motivation for using the in-process signals is to explore the relationship of these signals to temperature evolution, which can enable real-time prediction, control, and optimization.

Table 2 shows the two learned models $\mathcal{N}_{heat\_gen}(3)$ and $\mathcal{N}_{heat\_gen}(6)$ and their performance comparison. The best model structure column shows [3,8,1] (three input nodes, one hidden layer with eight nodes, and one output node) and [6,16,16,16,1] (six input nodes, three hidden layers each with sixteen nodes, and one output node) are chosen for $\mathcal{N}_{heat\_gen}(3)$ and $\mathcal{N}_{heat_{gen}}(6)$,

Table 2 Learned models and their performances for the heat generation network with two sets of input features

Learned model	Selected features						Metrics			
	Spindle speed	Spindle torque	Material feed rate	Feed actuator torque	Feed actuator force	Tool temperature	Best model structure	Training MSE	Validation MAPE	Test MAPE
$\mathcal{N}_{\text{heat\_gen}}(3)$	√		√			√	[3,8,1]	0.0003	0.0046	0.0076
$\mathcal{N}_{\text{heat\_gen}}(6)$	√	√	√	√	√	√	[6,16,16,16,1]	0.0001	0.0037	0.0050

Fig. 5 Temperature prediction of heat generation stage by $\mathcal{N}_{\text{heat\_gen}}(3)$ on the training, validation, and testing sets

respectively. This best model structure is selected by grid search (see Sec. 5.1) from nine candidates. It is seen that a simpler model structure is chosen for a model with fewer features and vice versa. This can be because fewer features include less information and could need a simpler model structure to avoid overfitting during validation. On the contrary, more features could need a more complicated model structure to avoid underfitting. Mean squared error (MSE) is used for training the neural network models, which measures the error between the logarithmically transformed prediction and measurement. The mean absolute percentage error (MAPE) is used for validating and testing the model performance on unseen data; it provides improved insight into the relative error compared to MSE. MAPE is evaluated by scaling the prediction and measurement to their original values. It can be seen that for all metrics of MSE and MAPE, $\mathcal{N}_{\text{heat\_gen}}(6)$ outperforms $\mathcal{N}_{\text{heat\_gen}}(3)$. While $\mathcal{N}_{\text{heat\_gen}}(6)$ is significantly better than $\mathcal{N}_{\text{heat\_gen}}(3)$ on the training set, the difference in performance decreases for the validation and testing sets. This shows the

balance between the model accuracy and the model complexity induced by features and structures. It is noted the total grid search training times for $\mathcal{N}_{\text{heat\_gen}}(3)$ and $\mathcal{N}_{\text{heat\_gen}}(6)$ are 6 min and 8 min, respectively.

Figures 5 and 6 display the prediction of tool temperature evolution for the heat generation stage on the training, validation, and testing sets by $\mathcal{N}_{\text{heat\_gen}}(3)$ and $\mathcal{N}_{\text{heat\_gen}}(6)$. It is seen that the predictions for both models provide good agreement with the measured data. From these time series predictions, the differences between $\mathcal{N}_{\text{heat\_gen}}(3)$ and $\mathcal{N}_{\text{heat\_gen}}(6)$ are slight. Good extrapolation capability is also observed.

Figure 7 shows temperature prediction for the cooling stage using the tool cooling network on the training, validation, and test sets. The predictions closely agree with the measurement data. It is understood that the cooling stage of the tool undergoes mainly conduction through the feedstock rod and convection to the air. The learned tool cooling network demonstrates its capability to accurately capture the combined effects of conduction and convection.

Fig. 6 Temperature prediction of heat generation stage by $\mathcal{N}_{\text{heat\_gen}}(6)$ on the training, validation, and testing sets
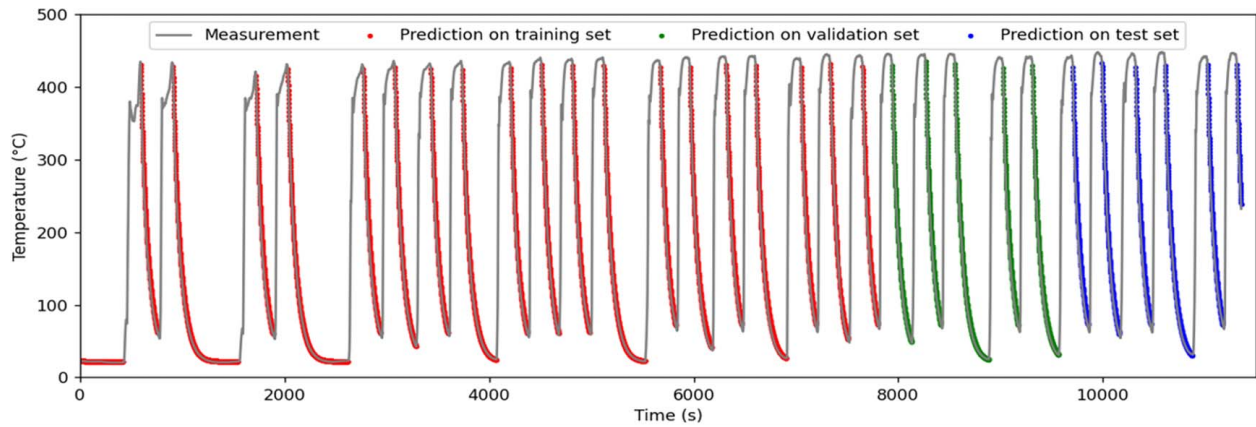
Fig. 7 Temperature prediction of cooling stage by tool cooling network on the training, validation, and testing sets

5.2.2 Model Validation for Build Temperature Evolution. The learned heat transfer network for the temperature evolution at the build is validated using the measurement data from the four thermocouples located in the substrate. Figure 8 displays the prediction results on the training and testing sets for the temperature at the four thermocouples in (*a*) to (*c*), respectively. It is seen that the predictions closely agree with the measurement data. Notably, Fig. 8(*d*) shows the extrapolation capability of the learned heat transfer network; the temperature prediction is accurate even though no data from thermocouple 4 is used in the training. Given any location on the build, its temperature evolution can be predicted. The good accuracy of the AFSD-Nets models enables the use of time domain simulation for further performance evaluation when predicting temperature evolution during AFSD.

5.3 Time Domain Simulation of Learned Models. This section presents the time domain simulation detailed in Algorithm 1 for both tool and build temperature evolution during AFSD using the validated models. The temperatures at time zero of the measurement data for the tool and the four thermocouples in the substrate are used as initial conditions for the simulation. The process decomposition is applied to determine which learned model should be used during simulation at any time. The time-step is set as 1 s. The simulation is completed over 11,358 steps to include all 30 layers of the deposition.

5.3.1 Time Domain Simulation for Tool Temperature Evolution. The heat generation network $\mathcal{N}_{\text{heat\_gen}}(3)$ uses only two process parameters and the time-delay tool temperature as inputs. Therefore, it can be used for time domain simulation in an offline fashion. Figure 9 displays the results of time domain simulation for tool temperature evolution using the coupled $\mathcal{N}_{\text{heat\_gen}}(3)$ and tool cooling network. In general, the simulation captures the trend of the temperature evolution at the tool for all layers, with a few exceptions at the peak temperatures during deposition. The first two layers are shown in Fig. 10. A shift to the left is observed. This is caused by the training data pre-processing to remove the first 20 measurements (a local temperature peak is observed at the virtual inlet) at each heat generation stage. During AFSD, the heating stage is typically longer with a newly filled feedstock rod as it is heated from room temperature. This causes a temperature reduction when the spindle speed is reduced from the peak value to the desired value for deposition. It is noted that for the coupled mode of time domain simulation, the accuracy of the heat generation network significantly impacts the tool cooling network by means of setting the initial conditions and vice versa. From this perspective, the learned models capture the underlying physics of the tool temperature evolution.

Similarly, Figs. 11 and 12 show the results for time domain simulation of the coupled heat generation network $\mathcal{N}_{\text{heat\_gen}}(6)$ and tool cooling network. $\mathcal{N}_{\text{heat\_gen}}(6)$ uses two process parameters and three in-process signals (spindle torque, feed actuator torque, and feed actuator force). Thus, it has the potential to be used for real-time applications; recall that the L3 controller can constantly provide in-process signals by its embedded sensors. It is seen that the deviations between the simulation and measurement at peak temperatures are reduced, showing the advantages of including in-process signal features for the model performance improvement.

5.3.2 Time Domain Simulation for Build Temperature Evolution. The tool temperature prediction by coupled simulation of the heat generation network $\mathcal{N}_{\text{heat\_gen}}(3)$ and tool cooling network is used as input to the heat transfer network to perform time domain simulation of the build temperature evolution. Figure 13 shows the results of this simulation. It is observed that the simulation generally captures the behaviors of the temperature evolution at build, including the thermal cycle and the trends of a time-dependent decrease of the peak temperatures and time-dependent increase in lowest temperatures as the wall height (and its thermal mass) increases. Figures 13(*a*) and 13(*b*) display some deviations from the measurement at the peak temperatures for the first 15 layers, while Figs. 13(*c*) and 13(*d*) accurately predict the peak temperatures. Lastly, Fig. 13(*d*) shows some non-smooth curves at the time epochs for process decomposition. This can be caused by the soft incorporation of discrete characteristics from the mask function in the current model structure, which may fail to recognize the underlying discrete patterns or disambiguate unrelated inputs.

The temperature predictions after 15 layers for all thermocouples are observed to deviate from the measurement. Potential explanations for this deviation are summarized into three key points: (a) All models are approximations of the ground truth. Neural networks have their limitations in approximating this complicated, multistage, and multi-physics AFSD process. (b) Time domain simulations have accumulated numerical errors. (c) Effective sensor measurements of the top layer (surface heat source) are not included, and only the sensor data at the tool head (single dot moving heat source) is available. Nevertheless, considering that only the initial values for the first two seconds are given, a complete 30-layer time domain simulation (11,358 steps) shows the superior performance of the proposed AFSD-Nets as it correctly captures the trend of thermal cycles and peak temperatures for most layers.

In addition, the tool temperature measurement is used instead as input for the heat transfer network to execute the time domain simulation. As shown in Fig. 14, it is observed that the deviations at the first 15 layers are significantly decreased. This indicates that integrating the in-process signals can have a great improvement on the simulation performance and can provide an accurate digital twin of the physical process for use in real-time prediction, control, and optimization.
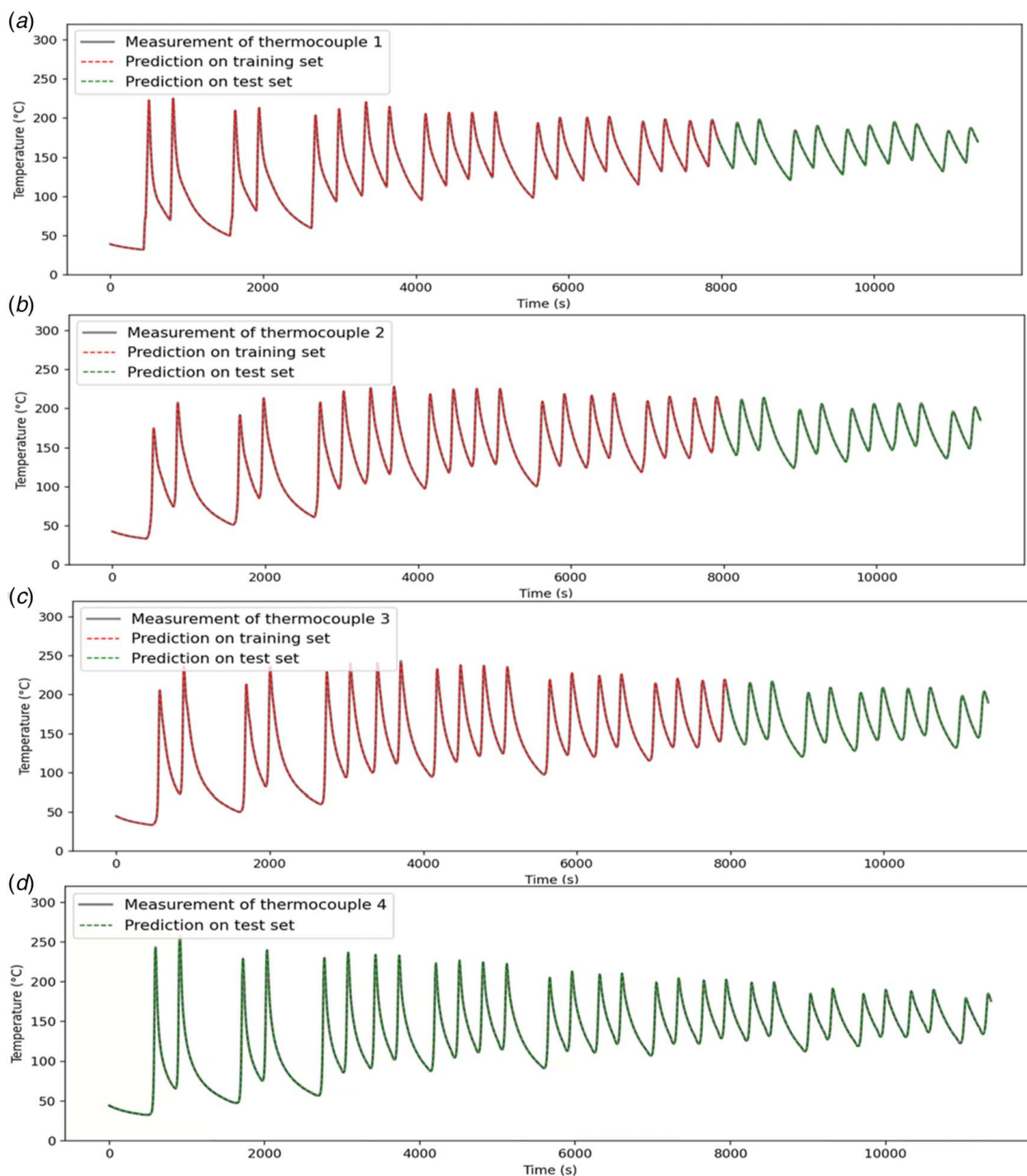
Fig. 8 Temperature prediction by the learned heat transfer network at the build on the training and testing sets. (*a*) to (*c*) represent the results for thermocouple 1 to 3, respectively, and (*d*) shows the extrapolation for thermocouple 4 prediction.

6 Additional Validations of AFSD-Nets and Its Acquired Models

In this section, additional validations for AFSD-Nets and its acquired models are presented to demonstrate superior performance in three ways: (1) In Sec. 6.1, numerical validation of AFSD-Nets versus non-physics-informed machine learning is presented; (2) Sec. 6.2 shows the results for a different training data size; (3) in Sec. 6.3, new experiments on a different spindle speed of 115 rpm are conducted, and the acquired models from the 135 rpm data are validated using the 115 rpm data. Note that all results reported in this section are sourced from time domain

simulations of the acquired models under comparison. In addition, for the build temperature, only the trajectory of thermocouple 4 is displayed since it is pure extrapolation.

6.1 Numerical Validation on Physics-Informed and Non-Physics-Informed Models. For this validation, the temperature evolution of the tool and build are respectively modeled by an individual NARX model. Compared with AFSD-Nets, the two networks $\mathcal{N}_{\text{heat\_gen}}(\cdot)$ and $\mathcal{N}_{\text{tool\_cool}}(\cdot)$ are combined as a single NARX for tool temperature modeling. The mask function in $\mathcal{N}_{\text{heat\_trans}}(\cdot)$ is also removed from the build temperature modeling.
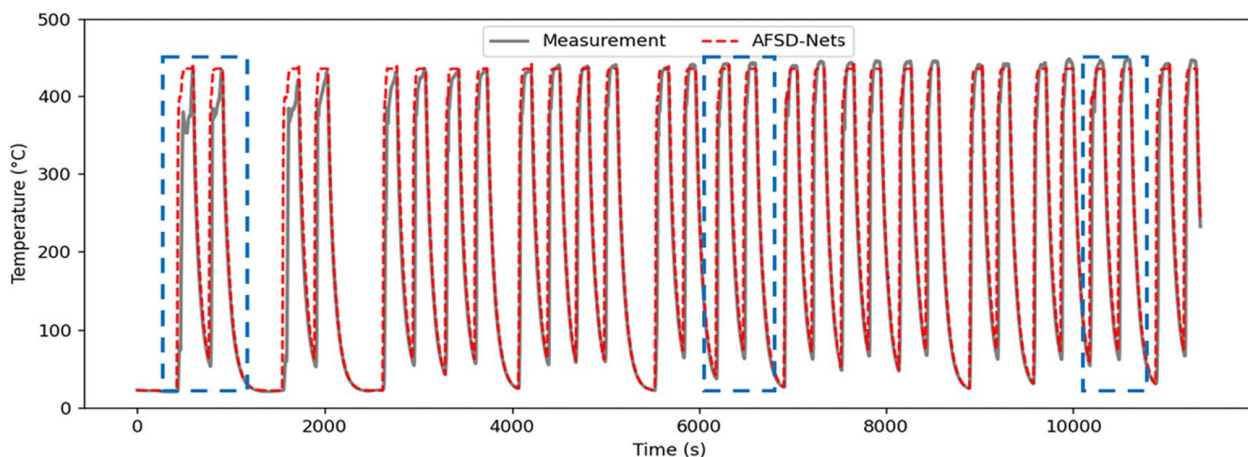
Fig. 9 Time domain simulation of tool temperature evolution by coupled $\mathcal{N}_{\text{heat\_gen}}(3)$ and tool cooling network with steady-state spindle speed of 135 rpm
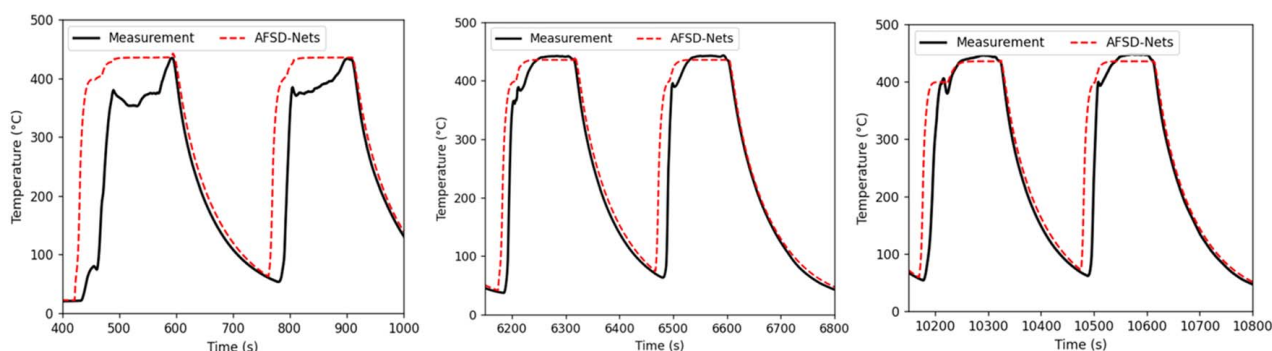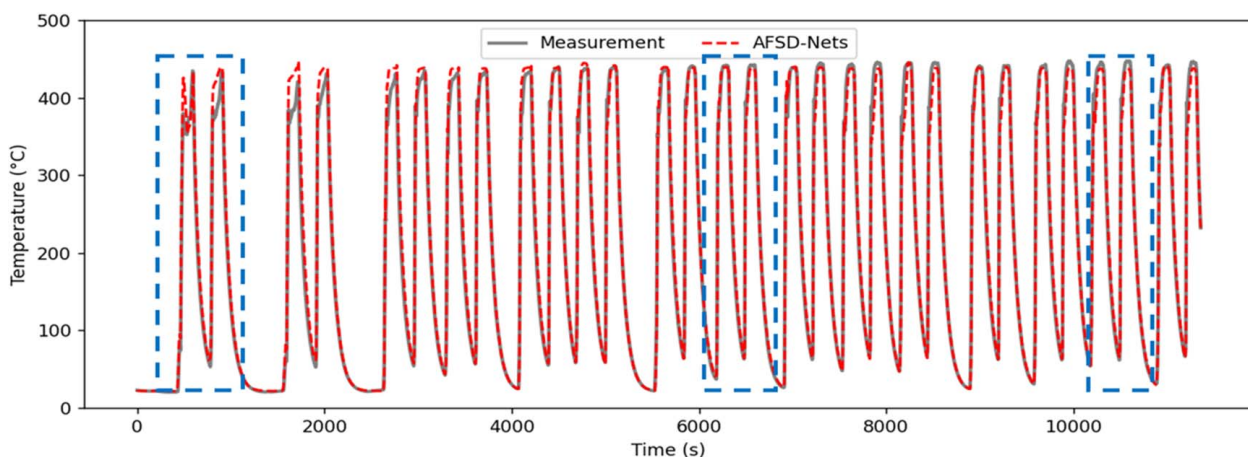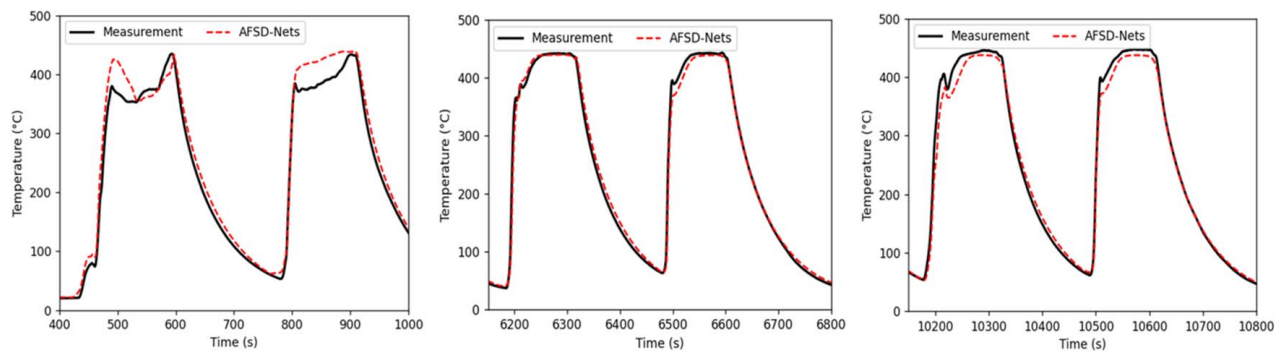

Fig. 10 The zoom in of the tool temperature evolution prediction in Fig. 9

In addition, the training data are not processed by physics-informed process decomposition. By using such settings, the NARX models are purely data-driven models that do not include physics-informed process decomposition of AFSD. Figure 15 shows the comparison results. The NARX model completely fails to model tool temperature evolution. For build temperature evolution, the NARX model has larger deviations from the measurements compared to AFSD-Nets. This validates that the proposed physics-informed machine learning approach, AFSD-Nets, can capture the underlying temperature evolution pattern of the AFSD process and thus it significantly outperforms the purely data-driven approach.

6.2 Numerical Validation on Different Training Data Sizes. A new setting for splitting the 30-layer deposition data is used as [10,10,10] in contrast to the original [20,5,5] setting in

Fig. 11 Time domain simulation of tool temperature evolution by coupled $\mathcal{N}_{\text{heat\_gen}}(6)$ and tool cooling network with steady-state spindle speed of 135 rpm

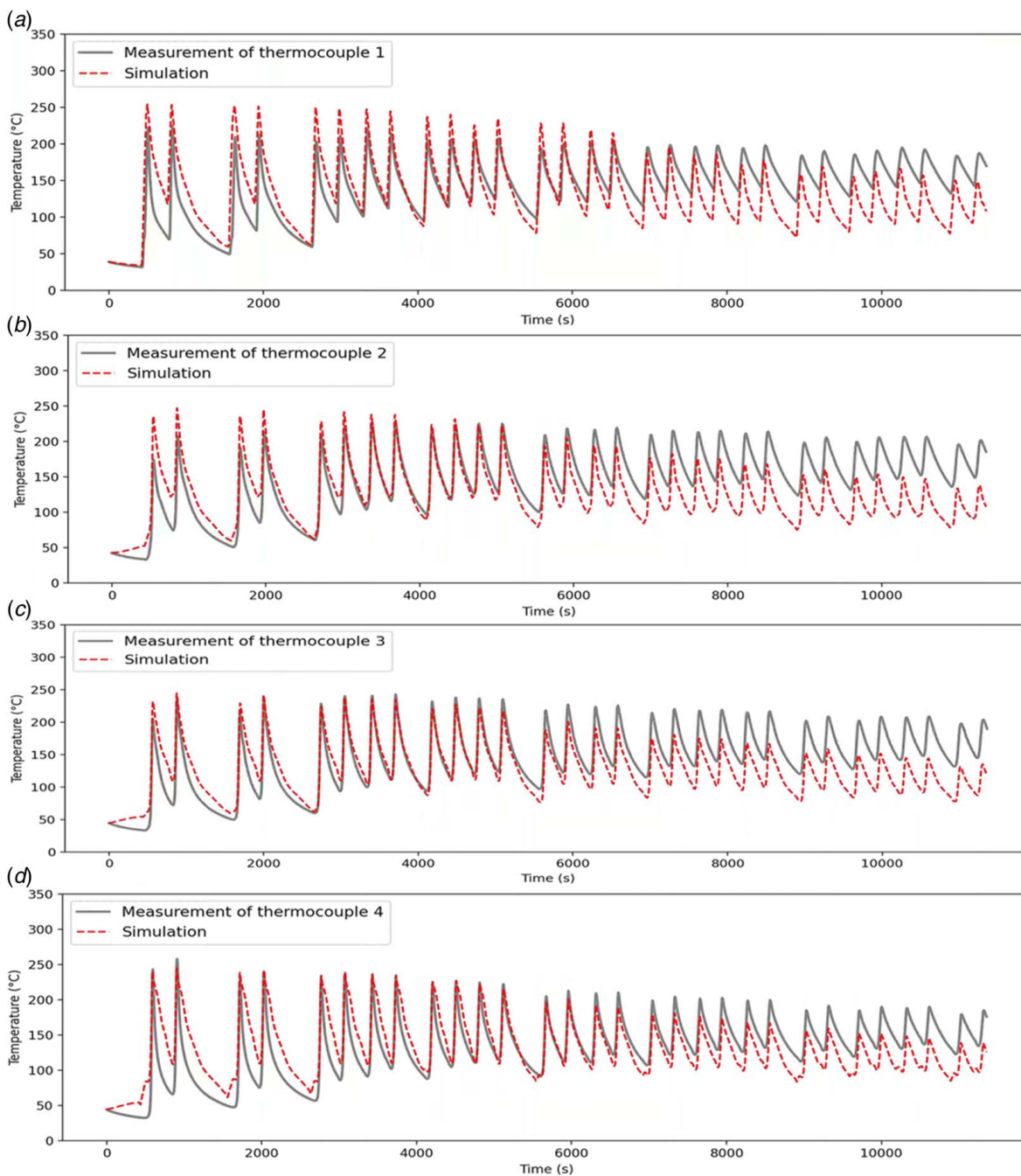**Fig. 12 The zoom in of the tool temperature evolution prediction in Fig. 11**

Fig. 13 Time domain simulation of build temperature evolution by coupled heat transfer networks. (*a*)–(*d*) show the results for prediction at thermocouples 1–4, respectively. The tool temperature prediction by coupled simulation of heat generation network $\mathcal{N}_{\text{heat\_gen}}$(3) and tool cooling network is used as input of heat transfer networks.
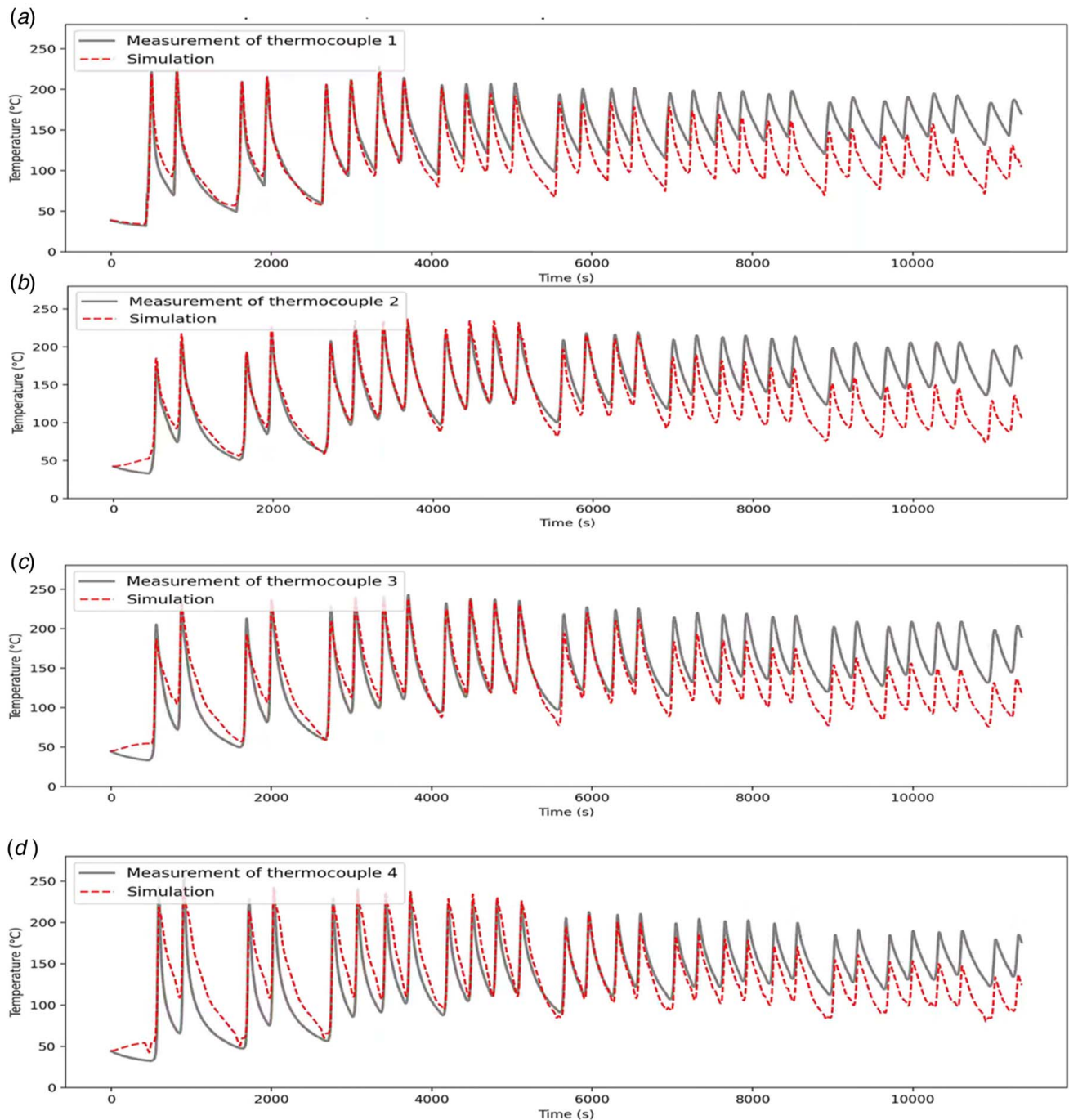
Fig. 14   Time domain simulation of build temperature evolution using the measured tool head temperature. (*a*)–(*d*) show the results for prediction at thermocouples 1–4, respectively. The measurement of tool temperature is used as input to the heat transfer networks.

Sec. 5. This new setting is used to validate the effectiveness of AFSD-Nets and the stability of the acquired models on different training data sizes. Figures 16(*a*) and 16(*b*) show the comparison results for tool and build temperature, respectively. For the tool, the model of [10,10,10] successfully captures temperature evolution and performs almost the same as that of [20,5,5]. For the build temperature, the model of [10,10,10] performs better than [20,5,5] for the first few layers and then worse than [20,5,5] for the last few layers. This is reasonable since the model of [10,10,10] is only trained using data from the first 10 layers. In general, both models are comparable. This validation shows that the proposed AFSD-Nets maintains stable performance for different training data settings.

6.3   Experimental Validation with Different Deposition Parameters. A critical issue with all ML approaches is their capability to extrapolate, that is, to predict beyond the data on which the ML models are trained. To validate the extrapolation capability of AFSD-Nets, additional physical experiments were performed using a spindle speed of 115 rpm while all other settings remained the same, as described in Sec. 4. The acquired models from AFSD-Nets using the data from a spindle speed of 135 rpm are directly used for the prediction of the measurements for the spindle speed of 115 rpm. Figure 17 shows good alignment between the simulation predictions and the measurements. The results demonstrate that the acquired AFSD-Nets models have strong extrapolation capability for the new spindle speed and can be potentially
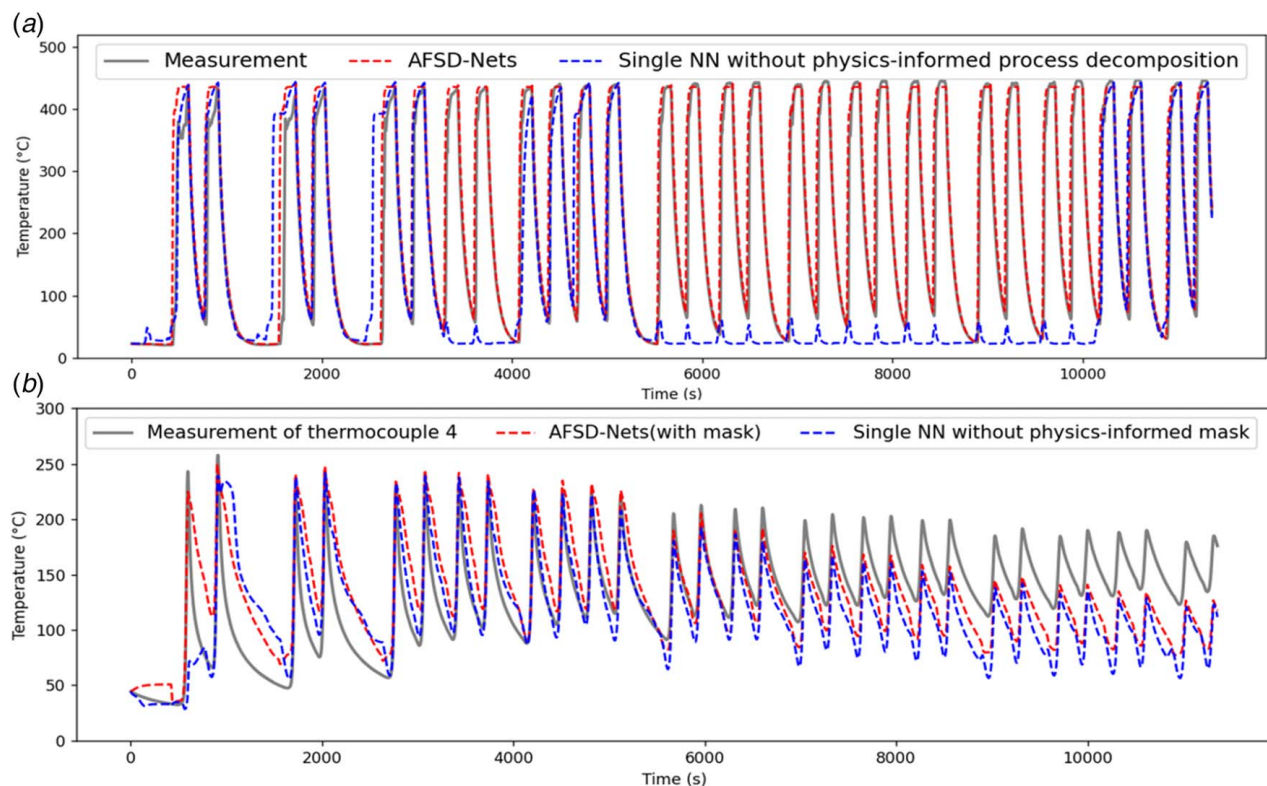
Fig. 15 Time domain simulation of tool and build temperature evolution by AFSD-Nets and a single NN without physics-informed process decomposition. (a) Simulation of tool head temperature evolution and (b) simulation of build temperature evolution.
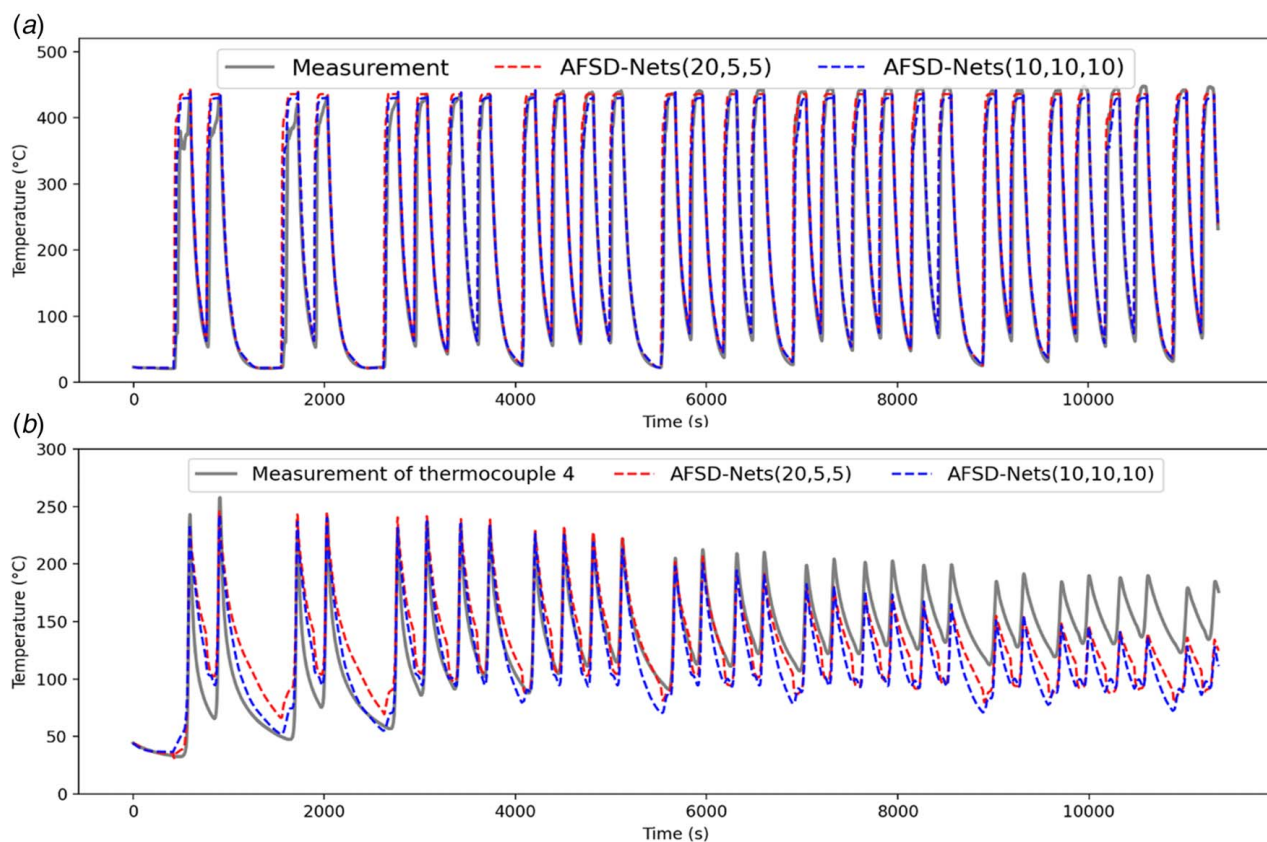

Fig. 16 Time domain simulation of tool and build temperature evolution by AFSD-Nets (20,5,5) and AFSD-Nets (10,10,10). AFSD-Nets (20,5,5) refers to the AFSD-Nets learned from the data with splitting of 20 training layers, 5 validation layers, and 5 test layers. (a) Simulation of tool head temperature evolution and (b) simulation of build temperature evolution.
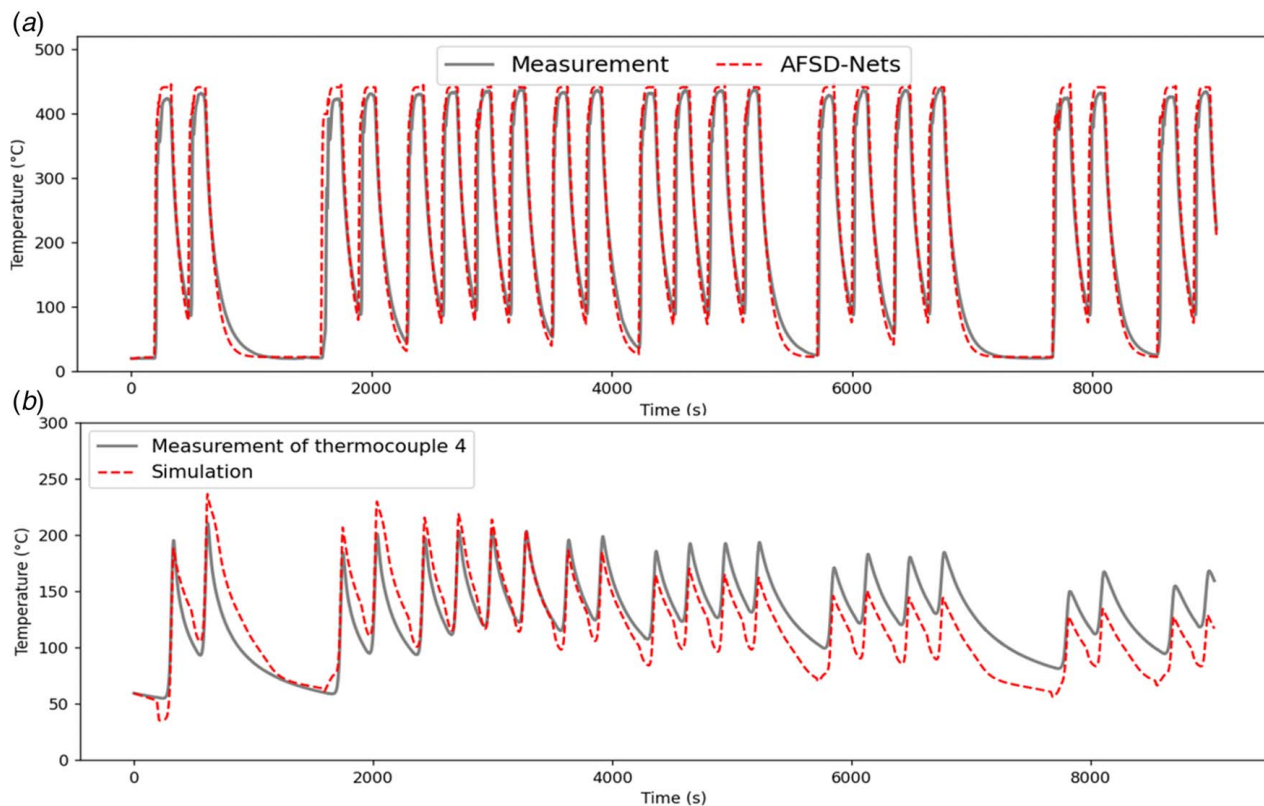
Fig. 17 Time domain simulation of tool and build temperature evolution given the steady-state spindle speed of 115 rpm. The AFSD-Nets obtained from the dataset of spindle speed of 135 rpm is directly utilized for simulating temperature evolution under the new setting of spindle speed. (a) Simulation of tool head temperature evolution and (b) simulation of build temperature evolution.

used for real-time predictions with other deposition settings in practice.

7 Conclusions and Outlook

This study presents a machine learning modeling effort for the temperature evolution of an emerging solid-state additive manufacturing process, additive friction stir deposition. The in-process signals are analyzed, and a process decomposition of the complete AFSD process is performed to generate multiple stages of heat generation and heat transfer. Based on this, a physics-informed machine learning approach, denoted as AFSD-Nets, is proposed to model heat generation and heat transfer by developing a set of neural networks, with each network modeling a distinct stage. For the tool temperature evolution, time-delay information and nonlinear autoregressive exogenous models are used for the modeling of heat generation and cooling, respectively. Heat generation models using process parameters only or process parameters and in-process signals as inputs are investigated. For the build temperature, the learned heat transfer network with a moving heat source is reused as an initial model for training the cooling network. Numerical results show good agreement of the learned models by AFSD-Nets to the experimental data. Time domain simulation is performed to demonstrate the effectiveness of the learned models by coupling them to predict the entire temperature evolution during AFSD. These results show the powerful capabilities of the proposed physics-informed machine learning approach to advance the understanding of the physical process of AFSD, as well as the potential to apply AFSD-Nets as the digital twin of AFSD temperature evolution using in-process data.

This study has two main limitations. The primary one is that the experimental data are from a single combination of process parameters, which limits the AFSD-Nets' ability to predict the behavior of different process parameters. Another one is the lack of interpretability of the learned models relative to the unknown governing equations. Future work will focus on designing a series of representative experiments to improve AFSD-Nets for the prediction of arbitrary process parameters, including tool spindle speed, material feed rate, and tool feed rate. In addition, the build geometry, tool path, and spatial temperature measurements will be utilized to enable AFSD-Nets to generate the 3D temperature distribution for a comprehensive description of the build temperature evolution. The interpretability of the learned models by AFSD-Nets will also be explored and enhanced to advance the understanding of the underlying physics during AFSD.

---

[2]http://energy.gov/downloads/doe-public-access-plan

Conflict of Interest

There are no conflicts of interest.

Data Availability Statement

The datasets generated and supporting the findings of this article are obtainable from the corresponding author upon reasonable request.

References

[1] Mishra, R. S., Haridas, R. S., and Agrawal, P., 2022, "Friction Stir-Based Additive Manufacturing," Sci. Technol. Weld. Joining, 27(3), pp. 141–165.

[2] Yu, H. Z., and Mishra, R. S., 2021, "Additive Friction Stir Deposition: A Deformation Processing Route to Metal Additive Manufacturing," Mater. Res. Lett., 9(2), pp. 71–83.

[3] Gopan, V., Wins, K. L. D., and Surendran, A., 2021, "Innovative Potential of Additive Friction Stir Deposition Among Current Laser Based Metal Additive Manufacturing Processes: A Review," CIRP J. Manuf. Sci. Technol., 32, pp. 228–248.

[4] Kincaid, J., Zameroski, R., No, T., Bohling, J., Compton, B., and Schmitz, T., 2023, "Hybrid Manufacturing: Combining Additive Friction Stir Deposition, Metrology, and Machining," TMS Annual Meeting & Exhibition, San Diego, CA, Mar. 19–23, Springer, pp. 3–13.

[5] Schmitz, T., Costa, L., Canfield, B. K., Kincaid, J., Zameroski, R., Garcia, R., Frederick, C., Rossy, A. M., and Moeller, T. M., 2023, "Embedded QR Code for Part Authentication in Additive Friction Stir Deposition," Manuf. Lett., 35, pp. 16–19.

[6] Kincaid, J., Charles, E., Garcia, R., Dvorak, J., No, T., Smith, S., and Schmitz, T., 2023, "Process Planning for Hybrid Manufacturing Using Additive Friction Stir Deposition," Manuf. Lett., 37, pp. 26–31.

[7] Dvorak, J., Gilmer, D., Zameroski, R., Cornelius, A., and Schmitz, T., 2023, "Freeform Hybrid Manufacturing: Binderjet, Structured Light Scanning, Confocal Microscopy, and CNC Machining," J. Manuf. Mater. Process., 7(2), p. 79.

[8] Schmitz, T., Corson, G., Olvera, D., Tyler, C., and Smith, S., 2023, "A Framework for Hybrid Manufacturing Cost Minimization and Preform Design," CIRP Ann., 72(1), pp. 373–376.

[9] Jin, Y., Yang, T., Wang, T., Dowden, S., Neogi, A., and Dahotre, N. B., 2023, "Behavioral Simulations and Experimental Evaluations of Stress Induced Spatial Nonuniformity of Dynamic Bulk Modulus in Additive Friction Stir Deposited AA 6061," J. Manuf. Processes, 94, pp. 454–465.

[10] Perry, M. E., Rauch, H. A., Griffiths, R. J., Garcia, D., Sietins, J. M., Zhu, Y., and Hang, Z. Y., 2021, "Tracing Plastic Deformation Path and Concurrent Grain Refinement During Additive Friction Stir Deposition," Materialia, 18, p. 101159.

[11] Zhu, N., Avery, D., Chen, Y., An, K., Jordon, J., Allison, P., and Brewer, L., 2023, "Residual Stress Distributions in AA6061 Material Produced by Additive Friction Stir Deposition," J. Mater. Eng. Perform., 32(12), pp. 5535–5544.

[12] Perry, M. E., Griffiths, R. J., Garcia, D., Sietins, J. M., Zhu, Y., and Hang, Z. Y., 2020, "Morphological and Microstructural Investigation of the Non-Planar Interface Formed in Solid-State Metal Additive Manufacturing by Additive Friction Stir Deposition," Addit. Manuf., 35, p. 101293.

[13] Griffiths, R. J., Garcia, D., Song, J., Vasudevan, V. K., Steiner, M. A., Cai, W., and Hang, Z. Y., 2021, "Solid-State Additive Manufacturing of Aluminum and Copper Using Additive Friction Stir Deposition: Process-Microstructure Linkages," Materialia, 15, p. 100967.

[14] Williams, M., Robinson, T., Williamson, C., Kinser, R., Ashmore, N., Allison, P., and Jordon, J., 2021, "Elucidating the Effect of Additive Friction Stir Deposition on the Resulting Microstructure and Mechanical Properties of Magnesium Alloy WE43," Metals, 11(11), p. 1739.

[15] Joshi, S. S., Patil, S. M., Mazumder, S., Sharma, S., Riley, D. A., Dowden, S., Banerjee, R., and Dahotre, N. B., 2022, "Additive Friction Stir Deposition of AZ31B Magnesium Alloy," J. Magnesium Alloys, 10(9), pp. 2404–2420.

[16] Beladi, H., Farabi, E., Hodgson, P. D., Barnett, M. R., Rohrer, G. S., and Fabijanic, D., 2022, "Microstructure Evolution of 316L Stainless Steel During Solid-State Additive Friction Stir Deposition," Philos. Mag., 102(7), pp. 618–633.

[17] Farabi, E., Babaniaris, S., Barnett, M. R., and Fabijanic, D. M., 2022, "Microstructure and Mechanical Properties of Ti6Al4 V Alloys Fabricated by Additive Friction Stir Deposition," Addit. Manuf. Lett., 2, p. 100034.

[18] Garcia, D., Hartley, W. D., Rauch, H. A., Griffiths, R. J., Wang, R., Kong, Z. J., Zhu, Y., and Hang, Z. Y., 2020, "In Situ Investigation into Temperature Evolution and Heat Generation During Additive Friction Stir Deposition: A Comparative Study of Cu and Al-Mg-Si," Addit. Manuf., 34, p. 101386.

[19] Hartley, W. D., Garcia, D., Yoder, J. K., Poczatek, E., Forsmark, J. H., Luckey, S. G., Dillard, D. A., and Hang, Z. Y., 2021, "Solid-state Cladding on Thin Automotive Sheet Metals Enabled by Additive Friction Stir Deposition," J. Mater. Process. Technol., 291, p. 117045.

[20] Avery, D. Z., Cleek, C., Phillips, B. J., Rekha, M., Kinser, R. P., Rao, H., Brewer, L., Allison, P., and Jordon, J., 2022, "Evaluation of Microstructure and Mechanical Properties of Al-Zn-Mg-Cu Alloy Repaired via Additive Friction Stir Deposition," ASME J. Eng. Mater. Technol., 144(3), p. 031003.

[21] Zeng, C., Ghadimi, H., Ding, H., Nemati, S., Garbie, A., Raush, J., and Guo, S., 2022, "Microstructure Evolution of Al6061 Alloy Made by Additive Friction Stir Deposition," Materials, 15(10), p. 3676.

[22] Phillips, B., Mason, C., Beck, S., Avery, D., Doherty, K., Allison, P., and Jordon, J., 2021, "Effect of Parallel Deposition Path and Interface Material Flow on Resulting Microstructure and Tensile Behavior of Al-Mg-Si Alloy Fabricated by Additive Friction Stir Deposition," J. Mater. Process. Technol., 295, p. 117169.

[23] Stubblefield, G., Fraser, K., Phillips, B., Jordon, J., and Allison, P., 2021, "A Meshfree Computational Framework for the Numerical Simulation of the Solid-State Additive Manufacturing Process, Additive Friction Stir-Deposition (AFS-D)," Mater. Des., 202, p. 109514.

[24] Stubblefield, G., Fraser, K., Van Iderstine, D., Mujahid, S., Rhee, H., Jordon, J., and Allison, P., 2022, "Elucidating the Influence of Temperature and Strain Rate on the Mechanics of AFS-D Through a Combined Experimental and Computational Approach," J. Mater. Process. Technol., 305, p. 117593.

[25] Stubblefield, G., Fraser, K., Robinson, T., Zhu, N., Kinser, R., Tew, J., Cordle, B., Jordon, J., and Allison, P., 2023, "A Computational and Experimental Approach to Understanding Material Flow Behavior During Additive Friction Stir Deposition (AFSD)," Comput. Part. Mech., 10(6), pp. 1629–1643.

[26] Kincaid, K. C., MacPhee, D. W., Stubblefield, G., Jordon, J., Rushing, T. W., and Allison, P., 2023, "A Finite Volume Framework for the Simulation of Additive Friction Stir Deposition," ASME J. Eng. Mater. Technol., 145(3), p. 031002.

[27] Gotawala, N., and Hang, Z. Y., 2023, "Material Flow Path and Extreme Thermomechanical Processing History During Additive Friction Stir Deposition," J. Manuf. Processes, 101, pp. 114–127.

[28] Joshi, S. S., Sharma, S., Radhakrishnan, M., Pantawane, M. V., Patil, S. M., Jin, Y., Yang, T., Riley, D. A., Banerjee, R., and Dahotre, N. B., 2022, "A Multi Modal Approach to Microstructure Evolution and Mechanical Response of Additive Friction Stir Deposited AZ31B Mg Alloy," Sci. Rep., 12(1), p. 13234.

[29] Sharma, S., Krishna, K. M., Radhakrishnan, M., Pantawane, M. V., Patil, S. M., Joshi, S. S., Banerjee, R., and Dahotre, N. B., 2022, "A Pseudo Thermo-Mechanical Model Linking Process Parameters to Microstructural Evolution in Multilayer Additive Friction Stir Deposition of Magnesium Alloy," Mater. Des., 224, p. 111412.

[30] Shao, J., Samaei, A., Xue, T., Xie, X., Guo, S., Cao, J., MacDonald, E., and Gan, Z., 2023, "Additive Friction Stir Deposition of Metallic Materials: Process, Structure and Properties," Mater. Des., 234, p. 112356.

[31] Merritt, G. R., Cousin, C. A., and Yoon, H.-S., 2024, "Nonlinear Temperature Control of Additive Friction Stir Deposition Evaluated on an Echo State Network," ASME J. Dyn. Syst., Meas., Control, 146(2), p. 021004.

[32] Karniadakis, G. E., Kevrekidis, I. G., Lu, L., Perdikaris, P., Wang, S., and Yang, L., 2021, "Physics-Informed Machine Learning," Nat. Rev. Phys., 3(6), pp. 422–440.

[33] Raissi, M., Perdikaris, P., and Karniadakis, G. E., 2019, "Physics-Informed Neural Networks: A Deep Learning Framework for Solving Forward and Inverse Problems Involving Nonlinear Partial Differential Equations," J. Comput. Phys., 378, pp. 686–707.

[34] Lu, L., Pestourie, R., Yao, W., Wang, Z., Verdugo, F., and Johnson, S. G., 2021, "Physics-Informed Neural Networks With Hard Constraints for Inverse Design," SIAM J. Sci. Comput., 43(6), pp. B1105–B1132.

[35] Brunton, S. L., Proctor, J. L., and Kutz, J. N., 2016, "Discovering Governing Equations From Data by Sparse Identification of Nonlinear Dynamical Systems," Proc. Natl. Acad. Sci. U. S. A., 113(15), pp. 3932–3937.

[36] Shi, Z., Ma, H., Tran, H., and Zhang, G., 2022, "Compressive-Sensing-Assisted Mixed Integer Optimization for Dynamical System Discovery With Highly Noisy Data," arXiv preprint arXiv:2209.12663.

[37] Sahoo, S., Lampert, C., and Martius, G., 2018, "Learning Equations for Extrapolation and Control," International Conference on Machine Learning, Stockholm, Sweden, July 10–15, PMLR, pp. 4442–4450.